Interplay between nonequilibrium quasiparticle relaxation and dynamic supercurrent enhancement in aluminum superconducting constriction junctions

Shung-Kang Koh [1], Pei-Yuan Li,[1] Ching-Ping Lee,[1] Io-Chun Hoi,[2] Yen-Hsiang Lin,[1] Chung-Yu Mou [1],
Dah-Chin Ling [3], Yung-Fu Chen [4], Cen-Shawn Wu,[5] and Jeng-Chung Chen [1]

[1]*Department of Physics, National Tsing Hua University, Hsinchu 30013, Taiwan*
[2]*Department of Physics, City University of Hong Kong, Tat Chee Avenue, Kowloon 999077, Hong Kong SAR*
[3]*Department of Physics, Tamkang University, Tamsui District, New Taipei City 25137, Taiwan*
[4]*Department of Physics, National Central University, Jhongli 32001, Taiwan*
[5]*Department of Physics, National Changhua University of Education, Changhua 50007, Taiwan*

We present a comprehensive study on the nonequilibrium properties of superconducting nanoconstriction junctions in steady-state and time-dependent dynamic regimes. By measuring the current-voltage characteristics of single constriction and micro-superconducting quantum interference devices with nanobridges, we observe a series of distinct voltage-step jumps in the dissipative state, which are associated with the appearance of the excess current. Through detailed analysis, we identify different mechanisms that contribute to the enhancement of superconductivity under varying bias voltages. In the time-dependent dynamic regime where the bias voltage V significantly exceeds the superconducting gap voltage ($V \gg \Delta/e$), the nanoconstriction behaves as a single phase-slip center (PSC). The voltage steps observed in this regime signify the phase-slipping dynamics at PSC, which effectively mitigates the self-heating effects. Conversely, in the steady-state regime where V is lower than the gap voltage, the voltage steps arise from multiple Andreev reflections. We demonstrate that the interplay of Andreev quasiparticles and Josephson supercurrent plays a crucial role in restoring the phase coherence of the dissipation currents. Our findings provide an insightful understanding of nonequilibrium quasiparticle relaxation dynamics in superconducting nanometallic weak links and offer practical implications for potential applications.

I. INTRODUCTION

Understanding the dynamics of superconducting (SC) weak links (WLs) is of great fundamental and practical importance for developing SC quantum interference devices and circuits [1]. WLs can be realized through various configurations, such as a tunnel coupling in a sandwich superconductor-insulator-superconductor (SIS) geometry, the proximity effects in a superconductor-metal-superconductor (SNS) geometry, or simply in the form of a short and narrow constriction, usually denoted as an ScS junction [2]. The investigation of nonequilibrium behaviors of these WLs under excess current biasing, including current carrying capabilities and the recovery processes back into SC states, provides a means to explore the internal activation and the relaxation dynamics of different types of WLs.

A significant focus in the field of nonequilibrium superconductivity has been geared towards investigating the nanoconstriction WLs in conjunction with two SC side banks. This research activity is primarily motivated by the development of superconducting quantum interference devices, such as Andreev qubits or μ-SQUIDs [3–5]. In these systems, Cooper pairs injected from one side bank are transformed into quasiparticles traveling through the constriction with a phase flipping along the WLs. This process is facilitated by the applied bias voltage V. Eventually, quasiparticles recombine to Cooper pairs on the other side [6,7]. A notable feature

observed in constriction WLs is that as the voltage is less than the gap voltage, $V < \Delta/e$, a new energy structure at submultiples of Δ emerges as a result of multiple Andreev reflections (MAR) between the contacts. This effect gives rise to a series of the differential conductance (dI/dV) features at $V = 2\Delta/em$, where m is an integer [3–5]. The overall current-voltage characteristics (IVC) exhibits a hysteretic feature: the WLs switch to a dissipative state when the bias current exceeds the critical current I_c and $V > 2\Delta/e$, whereas they restore to a zero-voltage state through the dynamics of the retrapping current $I_r (< I_c)$ during the current ramp-down process [8–12]. It is worth noting that the switching processes of both I_c and I_r are stochastic. The nature of hysteresis has been a subject of significant interest. It is generally believed that the hysteresis in ScS constriction junctions is of thermal origin, similar to that found in SNS junctions and unlike that of SIS WLs, wherein the hysteresis is understood in terms of an underdamped Josephson junction (JJ). The thermal hysteresis is attributed to the local Joule-heat dissipation within the constriction area, leading to the formation of a self-sustained hot spot [13–15], acting as a normal core or referring to a phase-slip center (PSC). Therefore, the hysteretic IVC can be conceptually modeled by a local thermal balance process dictated by the interplay of the hot PSCs and the cold SC banks.

Previous studies have mainly focused on investigations of nonequilibrium dynamics of the SC WLs in the long and

094512-1

dirty limits [2,8], leaving short SC WLs less explored. The dimension of short SC WLs, i.e., the constriction size, is comparable to that of a PSC, giving rise to the coexistence of a hot spot and a PSC at the center of the constriction where the phase and the order parameter of the supercurrent are substantially interrupted. Despite the fact that a number of models have been proposed in the last few decades to understand the hysteresis in SC WLs, the interplay between the contribution of heating and other nonequilibrium effects in short ScS WLs, crucial for practical applications, remains elusive. For instance, the operations of micron-size SQUID (μ-SQUID) can be hindered by the abrupt and stochastic nature of I_r switching. Moreover, earlier reports have shown that the magnetic flux (Φ_a)-dependent interference on μ-SQUIDs can only be observed in I_c, but never in I_r, implying that nonequilibrium quasiparticles lose phase coherence due to heating effects [15–17].

In this study, we investigate the dynamics of ScS WLs in the proximity of the short and clean limits, delineated as $\xi_0 \gg \ell \gtrsim (l, w, h)$, where ξ_0 represents the coherence length, ℓ is the mean free path, l denotes the length, w corresponds to the width, and h is the height of the constriction. We observe two distinct features in a hysteretic IVC: voltage snapback at $V > 2\Delta/e$ and MAR-correlated voltage staircase at $V < \Delta/e$. Furthermore, we find that the retrapping current I_r exhibits an oscillatory behavior with magnetic flux Φ_a in a μ-SQUID device, indicating that when quasiparticles are sufficiently cooled, superconducting phase coherence is not entirely suppressed by heating effects in the dissipative state of a thermally hysteretic Josephson device.

II. DEVICE FABRICATION

We develop a stable and reproducible technique to tailor a superconducting aluminum (Al) nanocontact junction by combining electron beam lithography (EBL) and focused ion beam (FIB). The method developed here can be incorporated with typical fabrication parameters of superconducting qubits.

Our first goal is to find accessible manipulation conditions of FIB to mill the facet of the Al layer, narrow the wire width, sculpt a cave below the wire, and finally make two chunks of Al electrodes in conjunction with a nanocube structure on the Si substrate. To find the parameters of FIB, including the ion energy and the angle of incidence to control the milling rates of Al and Si, we use the SRIM (Stopping and Range of Ions in Matter)/TRIM (TRansport of Ions in Matter) software package to simulate the moving and stopped recoiling atoms into the Si substrate and the Al layer [18]. It is known that the mean projected range of Ga$^+$ underestimates the cutting depth measured in the experiments. Previous reports demonstrated that the cutting depth in Si substrate is about 2.5 times larger than the implantation depth simulated [19]. We vary the number of Ga ions N from 50 to 1000 to simulate the increasing radiation damage exposure in FIB with dosage. Figures 1(a) and 1(b) show the representative calculation results of the TRIM simulation, where 300 of 30 kV Ga ions are implanted
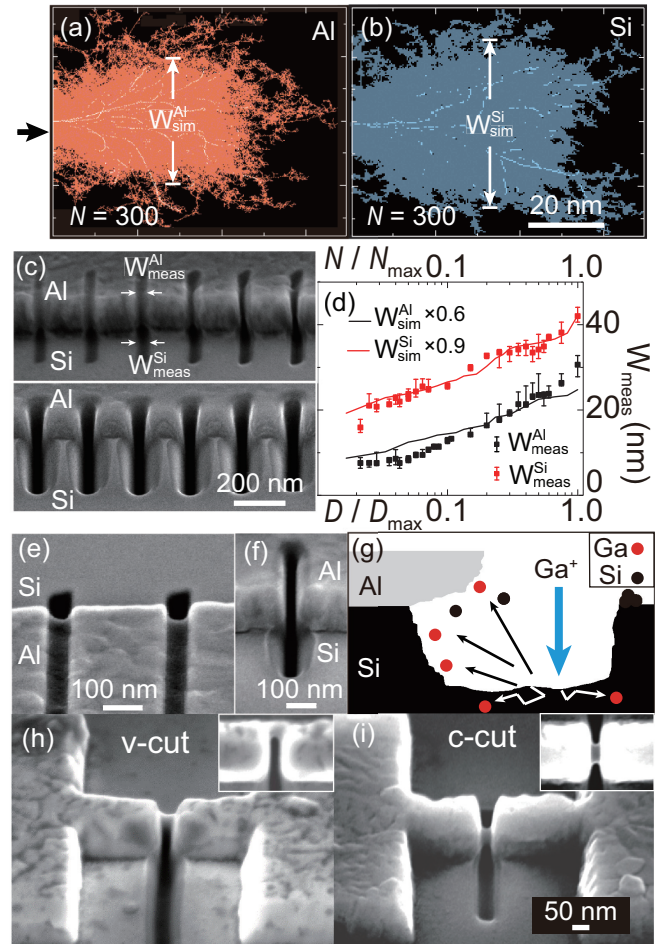

FIG. 1. Theoretical TRIM Monte Carlo simulations of gallium ions with 30 keV penetrating vertically (the black arrow) through the materials: (a) Al layer and (b) Si substrate under ion dosage of 6.12×10^{12} ions/cm^2. The milling width is estimated by the spreading width of Al/Si atom movement surrounding the incident area, denoted as $W_{\text{sim}}^{\text{Al}}/W_{\text{sim}}^{\text{Si}}$. (c) Transverse projection SEM image of a 150-nm-thick Al stripe on Si substrate after FIB milling, under ion dosages of 1×10^{13} ions/cm^2 to 1×10^{14} ions/cm^2 from left to right with a step increase of 3×10^{12} ions/cm^2. To have a clear view, the sample is titled by 52°. (d) The milling width measured by SEM image of the grooves along the boundary, denoted as W_{meas}, and obtained from SRIM simulation, denoted as W_{sim}, at different dosages (D) normalized to the maximum dose (D_{max}) of 1×10^{14} ions/cm^2. (e) The SEM image of the test device to illustrate the differential milling effect along the edge of the Al wire. (f) The SEM image of the redeposition effect of the sputtered Si atoms. (g) A schematic diagram to elaborate the differential milling effects between Al wire and Si substrate along the edge. The backscattered Ga$^+$ and Si effectively remove Al along the boundary and leave an undercut edge profile. We demonstrate two ways to sculpt the constriction by FIB: manipulating the ion beam to cut a thin Al wire from one side, named v-shaped cut (v-cut), or merely scanning over the wire, named c-cut. (h) and (i) Transverse projection SEM images of a v-cut and c-cut ScS junction, respectively. To obtain a clear view, the sample is tilted by 52°. The constriction region in the c-cut junction is directly Ga-implanted. The insets show the top view of the junctions.

vertically into the Al film and the Si substrate. The distributed elements show the movement of Al/Si atoms, and the light dotted lines display the trajectory of Ga ions. Here we take the widest spreading size of the moving Si and Al atoms, denoted as W_{sim}^{Si} and W_{sim}^{Al}, respectively, to evaluate the milling rate of the Al and Si materials. We note that both W_{sim}^{Al} and W_{sim}^{Si} tend to saturate when $N \geqslant 1000$.

Experimentally, we prepare a long stripe of Al film with a thickness of 150 nm deposited on Si substrate by EBL and manipulate the ion beam scanned across the edge of the Al film with the dose adopted from the simulations. Ion milling is performed using an FIB system equipped with a Ga$^+$ source (Helios Nanolab 450 S), operated at 30 kV and 1.1 pA, with a milling resolution of approximately 10 nm. Figure 1(c) shows the scanning electron microscope (SEM) image of the slices cut along the edge of the Al strip and Si substrate from which the width of the grooves can be determined, denoted as W_{meas}^{Al} and W_{meas}^{Si}. It is found that the widths of Si and Al increase with increasing dosage from 5 nm up to 25 nm for Al and 17 nm to 40 nm for Si as the ion dosage increases from 1×10^{13} ions/cm^2 to 1×10^{14} ions/cm^2. We summarize the width obtained from SRIM/TRIM simulations as a function of N (normalized to $N_{max} = 1000$) and the measured width as a function of normalized dose (D/D_{max}) in Fig. 1(d). By aligning N/N_{max} to D/D_{max}, we thereby establish empirical relations of $W_{meas}^{Al} \sim 0.6 \times W_{sim}^{Al}$ and $W_{meas}^{Si} \sim 0.9 \times W_{sim}^{Si}$, which allow us to design and fabricate ScS JJ with high reproducibility.

Figure 1(d) reveals that the difference between the milling width of the Si trench is approximately 20 nm larger than that of Al. This dosage-independent difference is confirmed with simulations. This variance suggests an enhanced milling effect on the edge, as shown in Fig. 1(e) with a dosage of 3×10^{13} ions/cm^2 in the planar view, where the Al film under ion bombardment is not only thinned down but is also inwardly removed by ~ 25 nm along the edge by sputtering. Figure 1(f) shows an alternative projected view on one groove, where the sputtered Si circularly redeposited around the trench can be clearly observed. We give a schematic illustration of how the milling process occurs on the edge in Fig. 1(g). The backscattered Ga$^+$ and Si effectively remove Al along the boundary and leave an undercut edge profile. This differential milling effect is found to be well reproduced. We, therefore, utilize it to perform precision milling of the specimen down to a nanoscale.

We prepare an Al-wire 150-nm-wide and 150-nm-thick by EBL and operate FIB to further narrow the wire to a nanocontact. We have tried two methods described in the following. We manipulate the beam to cut the wire from one edge toward the other and stop the beam at the edge as close as possible. In this process, a "v-cut" junction is formed, as shown in Fig. 1(h). Alternatively, we scan the beam across the wire with appropriate conditions, which allows us to fabricate a "c-cut" junction, as shown in Fig. 1(i). We encounter a technical problem in that the beam control needs to be more stable to have a high-yield production of the v-cut junction. On the other hand, the c-cut junction can be well reproduced. By scanning the ion beam across the wire, we can mill the facet of the Al layer down to ~ 90 nm, sculpt a cave below the substrate interface by Ga$^+$/Si sputters, and trim the wire to a
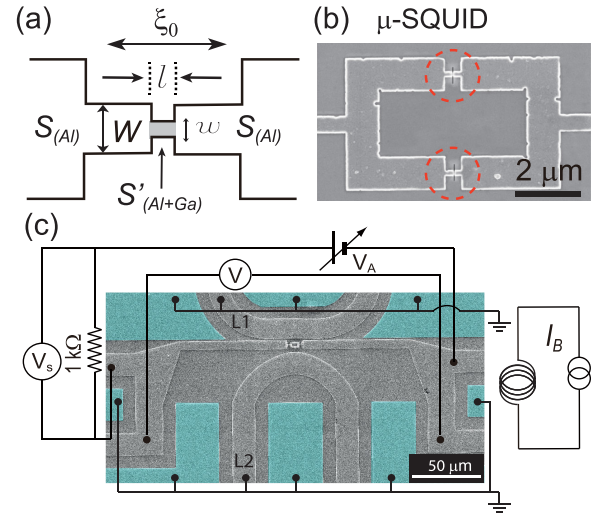

FIG. 2. The measurement setup of the Al-based ScS junction. (a) Schematic diagram of a single ScS junction studied, where the superconducting constriction region is Ga-implanted. (b) The magnified SEM image of the square SQUID device, consisting of two c-cut junctions marked by the red dashed circles. (c) The zoomed-out SEM image of the μ-SQUID device includes the current, voltage, and two on-chip flux-DC or -RF modulation lines, denoted as L1 and L2. The source and drive contacts are separated by approximately 200 μm. To avoid potential heating effects, L1 and L2 are grounded to the grounding pad, marked with false-color blue. We adopt an external superconducting coil to apply the global magnetic field.

narrow neck with a width of ~ 30 nm. Consequently, we are able to make a three-dimensional Al nanocube with a lateral size of ~ 25 nm $\times 30$ nm in contact with the chunk electrodes to form an ScS JJ. Data presented in the main text are mainly obtained from the c-cut ScS JJs.

III. MEASUREMENT SETUP AND DEVICE CHARACTERIZATIONS

We make two chunks of Al electrodes in conjunction with a nanocube structure with size $(l, w, h) \sim (25, 30, 75)$ nm, as schematically illustrated in Fig. 2(a). The constriction is locally implanted with Ga ions by using FIB. Note that its dimensions are comparable to the size of a single Al gain, which makes the Josephson device studied a heterointerface junction different from the homogeneous ScS junction investigated before [15,20,21]. The μ-SQUID device consists of one ScS in each branch.

Figures 2(b) and 2(c) show the enlarged SEM image of the μ-SQUID device studied, a zoom-out SEM image of a μ-SQUID, and a schematic diagram of the measurement circuit. The device layout was originally designed to perform rf measurements. Two transmission lines, L1 and L2, initially made for on-chip flux-tuning or sending rf excitations, are connected to the ground pads in the present work. All the experiments are conducted in a He3-refrigerator with a base temperature of ~ 0.3 K. We ramp a voltage V_A with a series resistor, and measure the bias current $I(=V_s/1 \text{ k}\Omega)$ and the voltage V across the junction. We place a nearby external superconducting coil to tune magnetic flux through the device
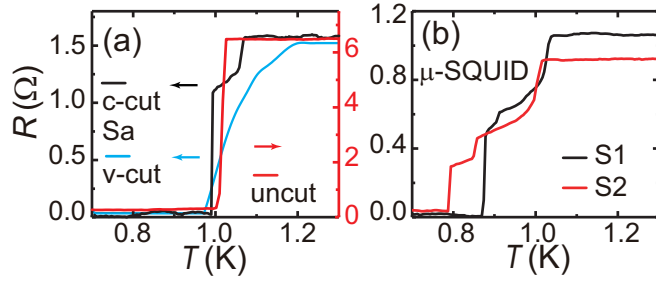
FIG. 3. (a) The temperature dependence (T) of the resistance (R) for an uncut Al wire and a single c-cut, denoted as Sa, and v-cut ScS junction. (b) $R - T$ curves of two μ-SQUIDs, labeled S1 and S2. The steplike features in $R(T)$ are attributed to different superconducting transition temperatures of the Al-bulk electrodes and the Ga-doped constrictions. In contrast to the c-cut device, the superconducting transition is relatively smooth in the v-cut device.

by applying current I_B. The IVC of the device is measured by a four-probe geometry, in which the measurement circuitry is adopted as a damper of environmental noise.

The temperature (T) dependence of the resistance (R) of five different samples, a single c-cut (Sa), v-cut junction, two μ-SQUIDs (S1, S2), and an uncut Al-wire are shown in Figs. 3(a) and 3(b), respectively. The superconducting transition width is sharp for Al wire with a critical temperature (T_c) around $\sim$1.02 K. The $R - T$ trace of Sa exhibits a step shoulder which broadens the transition width by $\sim$0.1 K, whereas multiple staircase features are observed for SQUID-type S1 and S2 devices. The step structures arise from the variance of T_c for different sections of the device: the chunk electrodes and two doped constriction regions [12,15,16,22], suggesting that the Ga$^+$ implanted region has a lower T_c. Note that the T_c onset of the v-cut JJ is $\sim$1.2 K, and R smoothly decreases to zero with a transition width of $\sim$0.15 K, which is wider than that observed in the uncut device. It suggests that the effect of Ga implantation on superconducting transition width in the v-cut JJ is far less than that of a c-cut ScS device. Based on the $R - T$ data, we estimate that the resistivity ρ_N of the constriction is approximately 1.35 $\mu\Omega$ cm at 4.2 K. Accordingly, the mean free path (ℓ) is approximately $\geqslant$ 5.9 nm [23,24]. In addition, the coherence length ξ_0 of device studied is estimated to be within $\sim$550–1600 nm, consistent with the tabulated value in Ref. [25]. Thus, the constriction junction fabricated is close to the clean and short limits.

IV. CURRENT-VOLTAGE CHARACTERISTICS

Figures 4(a), 4(b) and 4(c) display the representative IVC of Sa, S1, and S2, respectively. The arrows indicate the direction of the current sweep; a hysteretic IVC with the current ramping direction indicated by blue and red arrows. Upon increasing the current from zero, the device switches to a finite voltage state at I_c. When the current is ramped down from a value greater than I_c, the device regains its superconducting state at I_r. The general features of IVC aforementioned are well reproduced in all devices studied. The critical current I_c of Sa is approximately 0.6 mA which corresponds to the critical current density of $\sim$266 GA/m^2. The value is close
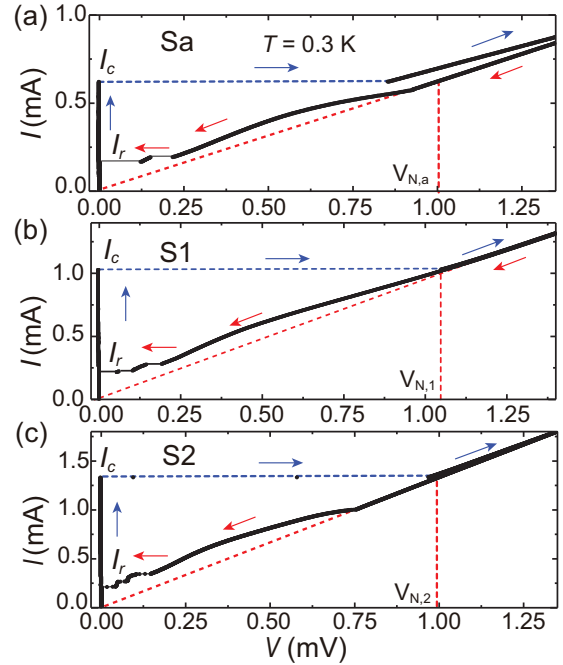

FIG. 4. $I - V$ characteristics of two types of devices: a single c-cut junction Sa and μ-SQUIDs S1 and S2, measured at 300 mK. (a) The full-scale $I - V$ curve of Sa. (b) and (c) The full-scale $I - V$ curve of S1 and S2. All $I - V$ curves are hysteretic. The blue and red arrows indicate the direction of the current sweep. The devices switch to a finite-voltage state at the critical current I_c and come back to a zero-voltage state at the retrapping current I_r.

to that of the bulk Al in the previous report [26], suggesting that the proximity effect enhances superconductivity in the Ga-doped constriction. The magnitude of I_c of S1 and S2 is approximately twice that of Sa. The IVC exhibits hysteretic switching behaviors for all devices. As the current is ramped down below I_c, the IVC deviates from linear dependence at $V \sim V_{N,i}$, as indicated by the vertical dashed line in Fig. 4, where i stands for the device index, e.g., $i = $ a for device Sa and $i = 1$, or 2 for S1 and S2, respectively. We extrapolate linear $I - V$ from the high-voltage end, e.g., $V > 2.5$ mV for S2 to the origin by a straight dashed line with slope $R_{N,i}^{-1} = I_c/V_{N,i}$. It is evident that the measured IVC is right on top of the extrapolated straight line at $V < V_{N,i}$, indicative of the existence of an excess current.

More importantly, the $I - V$ traces reveal three distinct features which can be classified by the voltages applied. In the high bias regime where $V > V_{N,i}$, successive voltage snapback steps are observed, as shown in Fig. 5. It should be noted that the upward current at a given V after the voltage snapback process is always larger than the downward current descending from higher voltages. Furthermore, these voltage steps consistently switch toward a lower voltage, which is equivalent to an increase in current ΔI_{sj} with $\Delta I_{sj}/I_c = 0.8 - 2.4\%$. This finding suggests that the consequence of the voltage snapback is to retain JJ in the superconducting state under excess driven current. In the low bias regime where $V < V_{n,i}$, the IVC exhibits staircaselike features, as illustrated in Fig. 6, before the current is reduced to the retrapping current I_r at
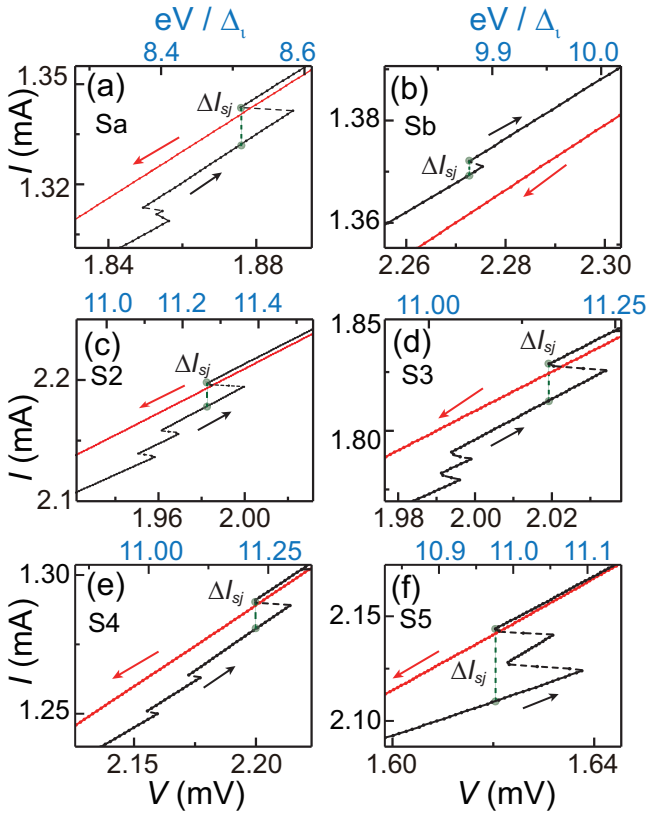
FIG. 5. The zoomed-in IVCs at $I > I_c$ show multiple voltage snapback features observed in single ScS Sa and Sb, μ-SQUIDs S2 to S5, respectively. The applied voltage normalized to Δ/e of each device is taken as the upper scale of the figure (see text for details). The green dashed line indicates an increase in current, denoted as ΔI_{sj}, after the voltage-snapback event.

which the devices studied regain the superconducting state. These stochastic switching features are correlated with MAR, which will be discussed in more detail later. In the middle bias regime where $V_{n,i} < V < V_{N,i}$, the excess current develops a bump in the IVC, as displayed in Fig. 4, resembling the so-called footlike structure observed in SC microbridges [2].

V. MAR-CORRELATED VOLTAGE-STEP JUMPS

To investigate the nature of the voltage steps, it is essential to determine a precise value of the gap voltage ($V = 2\Delta/e$). By assuming that two junctions of μ-SQUID are nearly identical, adopting the Ambegaokar-Baratoff relation: $I_c R_n = (\pi \Delta/2e) \tanh(\Delta/2k_B T)$ [2] and the Bardeen-Cooper-Schrieffer (BCS) $\Delta(T)$, and taking $\Delta(0)$ and R_n as fitting parameters to fit $I_c(T)$ for device Sa and S1 shown in Fig. 7(a), we find $\Delta_i \sim eV_{n,i}$ and the differential resistance $R_{N,i} = V_{N,i}/I_c$. To confirm these relations, we measure the temperature dependence of $V_{n,1}(T)$ of S1 and take $V_{n,1}(T) = \Delta_1(T)/e$ to plot $\Delta_1(T)/\Delta_1(0)$ as a function of T/T_c, as shown in Fig. 7(b). Our data are in good agreement with the BCS-type gap formula, suggesting that the value of the superconducting gap Δ_i can be reasonably determined by identifying $V_{n,i}$.

Figures 8(a)–8(f) show the full- and large-scale IVC with voltage normalized to $V_{N,i}$ for a single ScS JJ Sa and Sb
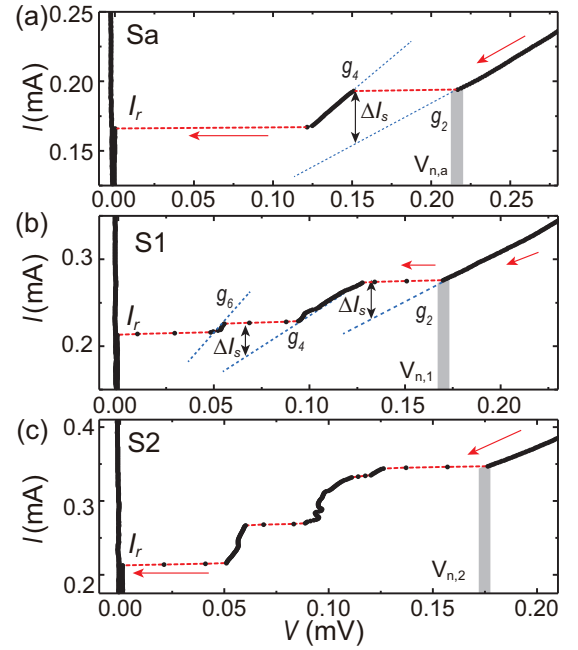
and μ-SQUIDs S1, S2, S3, and S4, respectively. Accordingly, Figs. 8(g) to 8(l) show the associated $dI/dV - V$ plot with the voltage normalized to $2\Delta_i$, where the red dashed lines, specifying the regime below which the staircaselike voltage switching takes place, are drawn for a guide to the eye. The peaks in dI/dV related to the threshold of voltage snapback switching in IVC occur at voltage $V = 2\Delta/em$, where $m = 2$ and 4 for single junction Sa and Sb, and $m = 2$, 4, and 6 for μ-SQUID S1 to S4. The switching voltage $2\Delta/em$ corresponds to the voltage at which the mth-order MAR process dominates. In general, the value of dI/dV increases with increasing m, as shown in Figs. 8(g)–8(l), suggesting that the voltage switching during a current down sweep is accompanied by an increase in the junction conductance. Moreover, the subgap differential conductance g ($\sim 1/R_n$) associated with coherent MARs of quasiparticles from the superconducting electrodes is larger

FIG. 6. The zoomed-in IVCs of Sa, S1, and S2 exhibit staircase features at $V \leqslant V_{n,i}$, where $V_{n,i}(T) = \Delta_i/e$. The voltage steps manifest the dynamic enhancement of the supercurrent, denoted as ΔI_s.
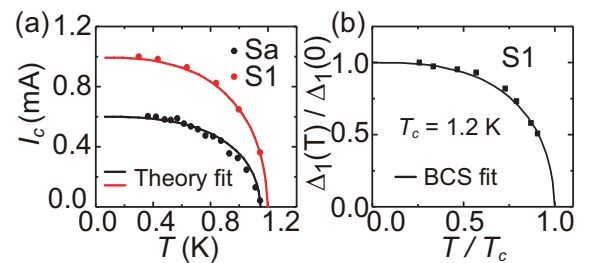

FIG. 7. (a) The temperature dependence of the critical current I_c for Sa and S1 (solid symbols). The curved lines are fitting results by using Ambegaokar-Baratoff relation. (b) Normalized superconducting gap as a function of temperature for S1, where the gap value is taken by $\Delta_1(T) = eV_{n,1}(T)$ and the solid line is a BCS fit.
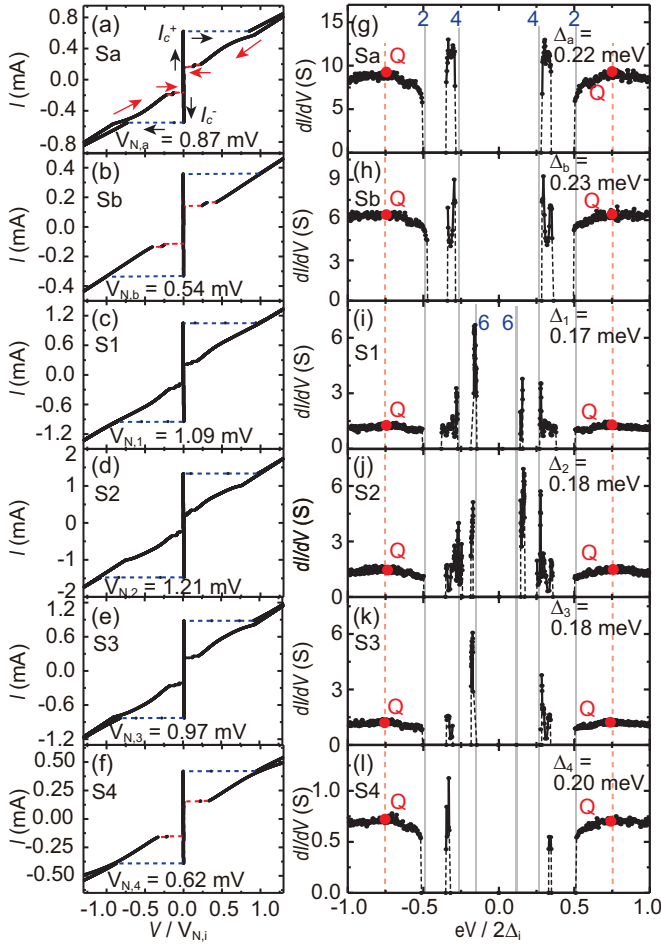
FIG. 8. The full-scale $I - V$ and the associated $dI/dV - V$ characteristics of Sa, Sb, and S1 to S4, measured at $T = 0.3$ K. (a) to (f) show the IVCs with V normalized to $V_{N,i}$ where $V_{N,i} = I_c R_N$, with $i = a$ to 4, respectively. The $dI/dV - V$ characteristics corresponding to (a) to (f) with V normalized to $2\Delta_i/e$ are displayed in (g) to (l), respectively. Note that dI/dV in the voltage switching process within the subgap regime cannot be analytically derived. Therefore, the dashed lines drawn are a guide for the eye. Each voltage step emerges at voltage $V = (2\Delta_i/em)$ with $m = 2$, 4, or 6. The Q point corresponding to the local maximum of footlike structure in $dI/dV - V$ is marked by a red solid circle consistently located at $\sim 0.75\,(eV/2\Delta_i)$ for the devices studied.

than that for $V > V_{n,i}$ ($\sim \Delta_i/e$), indicative of a dynamic enhancement of junction conductance arising from the voltage switching upon reducing the bias current.

Notably, our data measured from all devices studied reveal a remarkable coincidence once the applied voltage rescales with Δ_i/e. For example, the voltage steps below $V_{n,i}$ with $V = 2\Delta_i/em$ are intimately related to the MAR, the local maximum of a footlike structure marked "Q" point in Figs. 8(g)–8(l) consistently emerges around $\sim 0.75(eV/2\Delta_i)$, and the voltage steps above $V_{N,i}$ shown in Fig. 5 occur around $eV/\Delta_i = 9\sim 11$. As we will discuss below, the remarkable scaling feature is attributed to the constriction behaving as a single PSC, essentially carrying away the same amount of heat scaled with the gap energy Δ_i of each device studied.
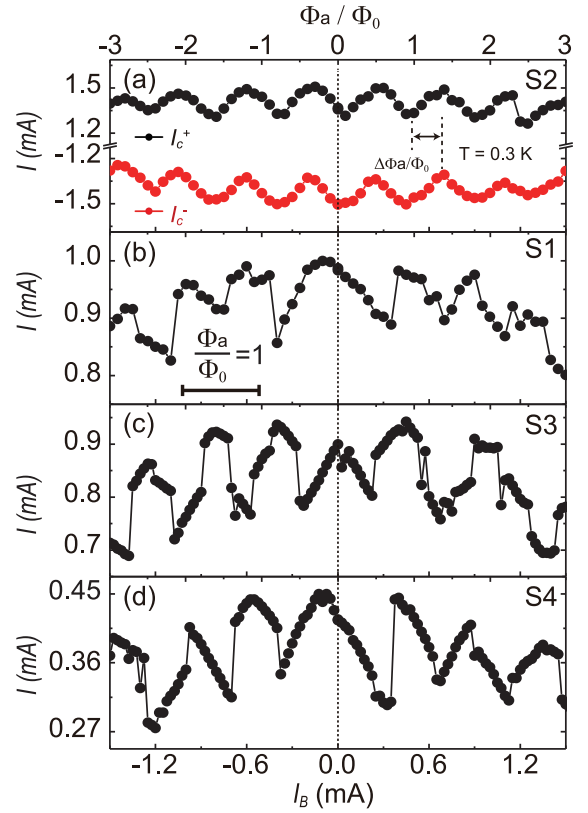

FIG. 9. Critical current I_c versus the normalized flux Φ_a/Φ_0 for four μ-SQUIDs S1 to S4 at $T = 0.3$ K. The applied flux Φ_a is controlled by the external coil current I_B. (a) The flux dependence of I_c^+ in the positive branch and I_c^- in the negative branch for S2. (b) to (d) The flux dependence of I_c^+ for the devices S1, S3, and S4. The current modulation depth to the flux quantum is approximately $200\ \mu A/\Phi_0$.

VI. THE FLUX DEPENDENCE OF THE SUPERCURRENT

In this section, we will present the flux dependence of the supercurrent in the μ-SQUID devices. The variations of the critical current I_c of the devices S1–S4 as a function of magnetic flux are shown in Fig. 9. By applying I_B to an external superconducting coil, as illustrated in Fig. 2, we measure the current-phase relation, $I_c(\Phi_a)$. Figure 9(a) shows the flux dependence of the maximum critical currents I_c^+ and I_c^- of S2 with a period of Φ_a/Φ_0, where $\Phi_0 = h/2e$ is the magnetic flux quantum.

The modulation of the critical current I_c by an applied magnetic field is approximately 10%, i.e., $\Delta I_c/I_c \sim 0.1$. As shown in Fig. 9(a), there is a phase shift, denoted as $\Delta\Phi_a/\Phi_0$, in $I_c(\Phi_a)$ between the forward and reverse bias directions. The reflection symmetry-breaking feature indicates that the two Josephson junctions in μ-SQUID S2 are asymmetric. As a result of the stochastic switching of I_c in μ-SQUIDs S1, S3, and S4, the $I_c(\Phi_a)$ of these devices deviates from the sinusoidal dependence illustrated in Figs. 9(b) to 9(d). However, this observation is qualitatively similar to the previous reports in Al nano-SQUIDs with long nanobridges and a large screening parameter [21,27]. The discontinuous current switching probably arises from flux-induced fluctuation effects. In addition, whether the doped Ga ions behaving as charged impurities in
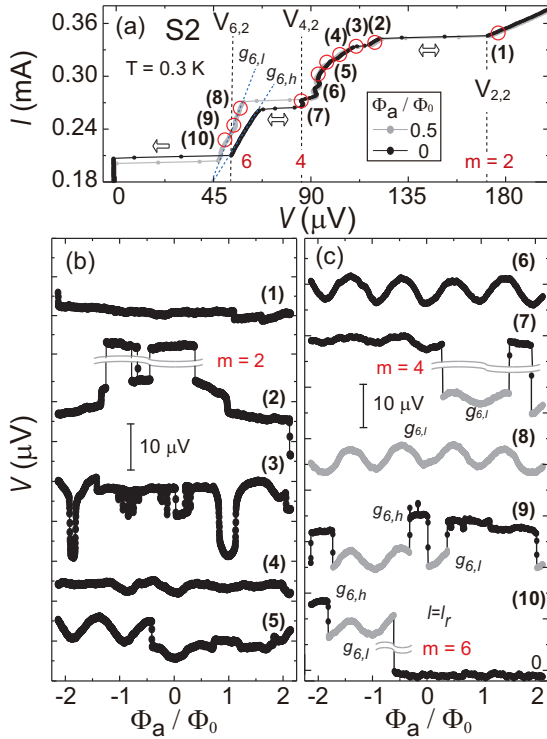
FIG. 10. (a) The $I - V$ characteristic of S2 in the presence of the normalized flux $\Phi_a/\Phi_0 = 0.5$ and 0 measured at 0.3 K. (b) and (c) Voltage modulation of S2 versus applied magnetic field at different bias currents, marked by the numbers indicated in (a). The data are offset for clarity.

the junction could be responsible for the bias-current-induced fluctuations is still an open issue.

We further explore the time-averaged DC supercurrent-phase relation $\bar{I}_s(\phi)$ in the dissipation region where MAR is present. The IVC of S2 at $V \leqslant \Delta/e$ with $\Phi_a = 0$ and $0.5\Phi_0$ is shown in Fig. 10(a). The threshold voltages of the mth-order MAR state are marked as $V_{m,2}$. Stochastic thermal bistability is observed between $V_{m,2}$ and $V_{m+2,2}$. We set the current I to the value marked by the numbers indicated in Fig. 10(a), continuously scan Φ_a from $-2\Phi_0$ to $2\Phi_0$, and display the data in Figs. 10(b) and 10(c). Discernible oscillations of $V(\Phi_a)$ in period of Φ_0 are found while $I < 0.3$ mA, i.e., below Point-(3), suggesting that $\bar{I}_s$ regains the phase coherence. These observations provide convincing evidence that the bias current I is dynamically distributed between the supercurrent $\bar{I}_s$ and the coherent normal current $\bar{I}_n$, i.e., $\bar{I}_n(\Phi_a) = I - \bar{I}_s(\Phi_a)$.

VII. DATA ANALYSIS AND DISCUSSION

The studies of the nonequilibrium SC phenomena can be tracked back to the 1970s (for review, see Refs. [2,8]). A dynamic equilibrium where superconductivity retains under dissipation in a nonequilibrium state can be established when the excitation from an external source is balanced by a relaxation process (for details see Ref. [2], chapter 11). The energy of the quasiparticles $E_k (= (\Delta^2 + \xi_k^2)^{1/2})$ depends on the SC order parameter $\Delta (= |\Delta|e^{i\phi})$, where ξ_k is the energy of an excitation at the momentum state k in the absence of the pairing interaction. In the dissipative state, the applied voltage drop
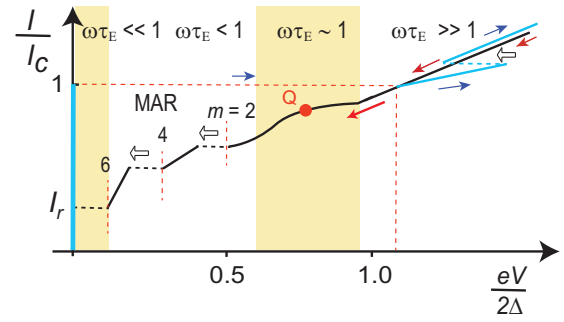

FIG. 11. Schematic $I - V$ curve of devices studied to elaborate distinct voltage switching features in three dynamic regimes characterized by a dimensionless parameter of $\omega\tau_E$.

across the constriction is associated with the change of the phase $\delta\phi$ taking place in one or several PSCs resided within, in accordance with the Josephson relation $\partial\phi/\partial t \sim V$. The external V alters the energy distribution of the quasiparticle excitations, $\delta f_k (= f_k - f_0)$, where f_k and f_0 is the excited and thermal-equilibrium Fermi function, respectively. The observable effects of disequilibrium δf_k depend on the interplay of the inelastic scattering time τ_{in} and the Josephson period $\tau_J(\sim 1/V \sim 1/I)$. Here, τ_{in} is correlated with the time variation of $|\Delta|$, governed by the energy-relaxation mechanisms. The relaxation rate is usually dominated by electron-phonon scattering; for example, τ_{in} (often denoted as τ_E) is on the order of 10^{-8} to 10^{-11} sec for Al.

Here we classify the observed features of IVC in different regions by using the parameter $\omega\tau_E$, where ω is the Josephson rate ($= 2\pi/\tau_J$), as depicted in Fig. 11 (not in scale). We start by discussing the condition at high voltages $V > V_N$ and $\omega\tau_E \gg 1$, where the rate of change of Δ is fast, and the injection rate is relatively high such that there is a rapid interchange of quasiparticles between the junction and the banks. As a result, the variation of quasiparticle occupation induces a voltage-switching event in a stochastic manner. Experimentally, the voltage steps similar to those observed in this study have been reported in a long superconducting filament [10] and bridge-type nano-SQUIDs [16], which can be understood within the framework of PSC [2]. The order parameter centered at PSC is driven to oscillate cyclically, and the phase rapidly slips, yielding a voltage across PSC and a time-averaged dc supercurrent ($\bar{I}_s$) [28,29]. The nonequilibrium current spreading over a region can be characterized by a charge-imbalanced distance (Λ), which can be approximately estimated by $dI/dV = (2\Lambda\rho_N/A)^{-1}$, where ρ_N is the normal-state resistivity, A is the cross-sectional area of the junction. We take the value of dI/dV from Fig. 8(i) at $V \sim 0.75(2\Delta/e)$ and estimate Λ of S1 to be approximately 8.3 nm. The fact that $l \sim \ell \sim \Lambda \ll \xi_0$ suggests that the perturbations of the phase and the order parameter are confined in the junction region. Therefore, the doped nanoconstriction can be treated as a single PSC, which effectively neutralizes the self-heating effects. As a result, our data reveal that the snapback features are consistently observed around $V = 9 - 11(\Delta_i/e)$, as indicated in the upper scale of Fig. 5, for all devices studied.

When the current is ramped down to the regime in which $\Delta/e < V < 2\Delta/e$, the I trace appears as a bump, in contrast

to the concave-up curvature expected from the resistively and capacitively shunted junction model [30]. This feature has been observed in SNS microbridges and is often referred to as footlike or shoulderlike structures [2,31]. It is generally believed that this feature is driven by the oscillations of $|\Delta|$ in the constriction region and not by the Joule dissipation $I^2 R_N$. Nevertheless, the kinetic mechanism is controversial: oscillations of $|\Delta|$ lead to the time-averaged "cooling" of the quasiparticles proposed by Ref. [31] and [2], but "heating" of the quasiparticles by Ref. [32]. In the "cooling" perspective, the bump signifies a nonequilibrium current enhancement. In the condition of $\omega \tau_E < 1$, the inelastic electron-phonon scattering tends to restore the equilibrium such that the cyclical oscillations of Δ give rise to an extra positive $\bar{I}_s$ up to voltages of order $\hbar/2e\tau_E$ ($\omega \tau_E \sim 1$) marked as the Q point in Figs. 8(g)–8(l). We estimate τ_E for S1 is about 10^{-12} s which is slightly smaller than the value reported in earlier reports [2] but is consistent with our claim that the constriction is disordered by the Ga dopant. As shown in Fig. 8, we find that the Q points consistently occur at ~ 0.75 (eV/$2\Delta_i$). The remarkable scaling of the snapback voltage and the Q point with Δ_i/e implies that the constriction region indeed behaves as a single PSC.

Alternatively, the "heating" perspective predicts that the footlike structure appears at a low voltage for the constriction with $w \geqslant l$ [32,33]. Reference [33] suggests that in such a geometry, the nonuniform current distribution induces a transition ($\propto 1/\tau_{in} \sim 1/\tau_E$) of the slow vortex motion at a low voltage to phase slip lines at a high voltage, resulting in an IVC resembling the footlike structure. The geometry of the constriction of our device [see Fig. 2(a)] meets the condition prescribed. However, due to smaller τ_E of the Ga-doped constriction, we cannot observe a hyperboliclike IVC as T is elevated near T_c, as predicted in Ref. [33]. In any case, more studies are needed to clarify the issues of these two pictures.

We proceed to consider the case of $V \leqslant 2\Delta/e$, or $\omega_J \tau_E \leqslant 1$, where the nonequilibrium state is mediated by Andreev quasiparticles. The red dashed lines in the IVC shown Fig. 4 represent $V = R_N I$, where R_N is the normal-state resistance of the device. The voltage asymptote lies above the normal-state characteristics, suggesting the appearance of excess current. The voltage-dependent excess current I_{exc} is defined as $I_{exc} = I(eV/\Delta \gg 1) - V/R_N$ and is often referred to as the additional current at a large V in the SNS junction, stemming from Andreev reflections [6]. In terms of Blonder, Tinkham and Klapwijk theory [34], R_N can be characterized by $R_N = R_0 (1 + 2Z^2)$, where Z is a dimensionless scattering parameter modeling the inelastic scattering at the interface, $R_0 = [2A v_F e^2 N(0)]^{-1}$, and $N(0)$ is the density of states at the Fermi energy. It predicts that Andreev reflections increase I_{exc} with lowering the voltage at a smaller $Z(\leqslant 1)$ and I_{exc} increases with decreasing Z. The general trend of increasing excess current while increasing g with increasing the mth-order MAR state, shown in Figs. 4 and 6, qualitatively agrees with that proposed for SNS microbridges.

The correlation between the subgap structure and the excess current with MAR has been investigated for years. The related studies recently resurged because of the search for Majorana quasiparticles [35]. A superconductor-topological insulator-superconductor (S-TI-S) junction or a

superconductor- nanowire-superconductor (S-NW-S) junction is considered a platform to host Majorana fermions [36–46]. A wide variety of IVC of the above-mentioned SC junctions have been experimentally observed, which makes a detailed comparison with theoretical studies precluded. Understanding IVC requires careful scrutiny of the junction properties. For example, the MAR can be so effective that the extrapolated value of I_{exc} at $V = 0$ is larger than I_c for the junction made of topological insulator materials [36,37]. In contrast, this extrapolated I_{exc} nearly vanishes for nanobridge or quasi-one-dimensional WLs [4,14,15]. In other instances, the subgap structure is only sometimes visible despite the presence of a large I_{exc} [4,38].

To understand the nature of the MAR-correlated step feature at $\omega_J \tau_E \leqslant 1$, we need to take into account thermal hysteresis, namely, quasiparticle heating in the constriction. There are several thermal models for understanding the hysteretic IVC of short SC WLs and μ-SQUIDs with the geometry similar to that of the devices studied [7,12,32,47]. A typical thermal model considers the Joule heat near the WL region in the dissipative state to be removed in two ways: conduction within each electrode and the surface heat flow from the film's bottom surface to the substrate [12]. Furthermore, experimental studies have shown that electronic thermal conduction and phonon conduction dominate the heat removal processes in a short and a long JJ, respectively [14]. In our short constriction JJ, the formation of Andreev bound states produces pronounced local density of states [7], which facilitates the heat transport either in the kinetic equation of f_k described by the time-dependent Ginzburg-Landau equation [32] or the electronic thermal conduction proposed by the thermal model [12]. Either model can qualitatively account for voltage jump accompanied by increasing g as MAR takes place.

As $\omega \tau_E \ll 1$, i.e., $\tau_J \gg \tau_E$, the V applied is much smaller than Δ/e, and the oscillation period of $|\Delta|$ is much longer than τ_E. The relaxation will occur quickly on the scale of τ_J. The nonequilibrium quasiparticle relaxation predominantly damps the phase-slip process, resulting in the emergence of the re-trapping current below which Joule heating is insufficient to sustain a temperature above T_c. Consequently, the dynamic phase-flip process ceases at $I = I_r$.

Finally, we emphasize that regardless of the voltage steps observed at $V > 2\Delta/e (I > I_c)$ or $V \leqslant \Delta/e$, the voltage jumps from a higher to a lower value while keeping the current unchanged is equivalent to a reduction in the junction resistance or an enhancement of superconductivity by increasing $\bar{I}_s$. Therefore, the occurrence of the voltage steps is the signature of the dynamic enhancement of superconductivity. We estimate the level of enhancement corresponding to a shift of the nonequilibrium temperature $\delta T^* = -0.01 T_c$, which is quantitatively consistent with previous works [2]. The supercurrent-phase relation $\bar{I}_s(\phi)$ shown in Fig. 10 confirms our claim of the superconductivity enhancement effect assisted by MAR in the dissipative state.

VIII. CONCLUSION

To conclude, we develop a scheme utilizing FIB technique to fabricate a locally doped superconducting nanoconstriction junction. We find the voltage-step features emerged in two

distinct regimes: the voltage far above Δ/e due to the dynamics of the phase-slip center and the voltage below Δ/e mediated by MAR. Both the voltage snapback and the staircaselike voltage switching manifest a dynamic enhancement of supercurrent to regain the superconductivity in JJ. In the μ-SQUID device, we observe a modulation of the retrapping current as a function of the magnetic flux through the loop with a period of Φ_0, suggesting that the higher-order MAR of nonequilibrium quasiparticles can preserve superconducting phase coherence while quasiparticles are sufficiently cooled. Our work extends the present understanding of nonequilibrium superconductivity near the clean and short limits and will stimulate further theoretical investigations in this rapidly evolving field.

APPENDIX: ANALYSIS OF DEVICE CHARACTERISTICS WITH RCSJ MODEL

It is well-established that the dynamics of Josephson junctions can be quantitatively analyzed in the framework of resistively and capacitively shunted junction (RCSJ) model [2,30]. Within the RCSJ model, the junction dynamics can be characterized by the Stewart-McCumber parameter $\beta_c(= (\omega_c/\omega_p)^2 = \omega_c/\omega_{RC})$, where $\omega_c = 2\pi I_c R_n/\Phi_0$ is the Josephson frequency at voltage $V_c \equiv I_c R_n$, $\omega_p = (2\pi I_c/\Phi_0 C)^{1/2}$ is the plasma frequency, and $\omega_{RC} = 1/R_n C$. In the limit of $\beta_c \gg 1$, called the underdamped limit in which the time for the phase to change is extremely short compared to that for the charge to relax from the capacitor. Consequently, the

TABLE I. Summary of key characteristics of the devices.

Sample	$V_{N,i}$ (mV)	I_c^+ (mA)	$R_{n,i}$ (Ω)	$\Delta_i(0)$ (meV)	β_c	β_L	C_i (pF)	L_i (pH)	ω_c (THz)
Sa	0.827	0.59	1.396	0.193	21.2	–	6.08	–	2.50
Sb	0.535	0.345	1.668	0.23	11.3	–	3.87	–	1.75
S1	1.064	1.032	1.073	0.192	70.0	7.51	21.4	7.53	3.62
S2	1.207	1.332	0.904	0.176	71.1	9.55	15.1	7.42	4.37
S3	0.911	0.883	0.883	0.189	22.9	9.18	6.93	10.8	2.97
S4	0.621	0.421	1.702	0.219	12.0	4.29	3.24	10.6	2.17
S5	1.000	2.073	0.481	0.094	8.91	–	6.12	–	3.03

dynamics of the junctions are governed by the parallel combination of the $R - C$ circuit, resulting in an average dc voltage of $V \sim I_c R$ during the process upon which the dc bias current increases from zero to I_c. As the current I is reduced below I_c, V does not switch back to zero until a retrapping current I_r is reached, where $I_r/I_c = 4/(\pi\sqrt{\beta_c})$ for $\beta_c \gg 1$ in the absence of fluctuations [30]. To quantify the relevant parameters, we adopt this expression to determine β_c and C of devices studied. As a result of I_r much smaller than I_c in experimental data, the extracted value of β_c is greater than one, indicating that the devices studied are classified as underdamped junctions. Moreover, the screening parameter $\beta_L(= 2LI_c/\Phi_0)$, where L is the inductance of the loop, can be deduced from the suppression of the critical current by field modulation. In the case of $\beta_L \gg 1$, $\Delta I_c(\Phi)/I_{c(max)} \sim 1/\beta_L$ [2,30]. We can, therefore, extract β_L and L of device studied from $\Delta I_c(\Phi)/I_{c(max)}$ data. Based on the length and the ratio of the rectangular hole of the SQUID [48], we estimate the inductance L of the device studied, for example, S2, to be ~ 7.39 pH, which is self-consistent with the value of ~ 7.42 pH obtained from the above-mentioned scheme. Furthermore, the penetration depth λ_L is estimated to be approximately 40–50 nm, and the Fermi wavelength $\lambda_F \sim 0.4$ nm [25]. With $w \gg \lambda_F$, the constriction is a multichannel mesoscopic system for quasiparticle transport. Finally, the key parameters of the devices studied are summarized in Table I for references.

[1] M. H. Devoret, J. M. Martinis, and J. Clarke, Phys. Rev. Lett. **55**, 1908 (1985).

[2] M. Tinkham, *Introduction to Superconductivity* (McGraw-Hill, New York, 1996).

[3] A. Levy Yeyati, A. Martín-Rodero, and F. J. García-Vidal, Phys. Rev. B **51**, 3743 (1995).

[4] N. van der Post, E. T. Peters, I. K. Yanson, and J. M. van Ruitenbeek, Phys. Rev. Lett. **73**, 2611 (1994).

[5] A. Martín-Rodero, F. J. García-Vidal, and A. Levy Yeyati, Phys. Rev. Lett. **72**, 554 (1994).

[6] K. Flensberg, J. B. Hansen, and M. Octavio, Phys. Rev. B **38**, 8707 (1988).

[7] A. Gumann, T. Dahm, and N. Schopohl, Phys. Rev. B **76**, 064529 (2007).

[8] K. K. Likharev, Rev. Mod. Phys. **51**, 101 (1979).

[9] R. Tidecks, *Current-Induced Nonequilibrium Phenomena in Quasi-One-Dimensional Superconductors* (Springer, Berlin, 1990).

[10] W. J. Skocpol, M. R. Beasley, and M. Tinkham, J. Appl. Phys. **45**, 4054 (1974).

[11] M. Tinkham, J. U. Free, C. N. Lau, and N. Markovic, Phys. Rev. B **68**, 134515 (2003).

[12] D. Hazra, L. M. A. Pascal, H. Courtois, and A. K. Gupta, Phys. Rev. B **82**, 184530 (2010).

[13] H. Courtois, M. Meschke, J. T. Peltonen, and J. P. Pekola, Phys. Rev. Lett. **101**, 067002 (2008).

[14] P. Li, P. M. Wu, Y. Bomze, I. V. Borzenets, G. Finkelstein, and A. M. Chang, Phys. Rev. B **84**, 184508 (2011).

[15] N. Kumar, T. Fournier, H. Courtois, C. B. Winkelmann, and A. K. Gupta, Phys. Rev. Lett. **114**, 157003 (2015).

[16] D. Hazra, J. R. Kirtley, and K. Hasselbach, Phys. Rev. Appl. **4**, 024021 (2015).

[17] S. Paul, G. Kotagiri, R. Ganguly, H. Courtois, C. B. Winkelmann, and A. K. Gupta, Phys. Rev. Appl. **15**, 024009 (2021).

[18] J. F. Ziegler, Nucl. Instrum. Methods Phys. Res. Sect. B **219-220**, 1027 (2004).

[19] Z. W. Xu, F. Z. Fang, Y. Q. Fu, S. J. Zhang, T. Han, and J. M. Li, J. Micromech. Microeng. **19**, 054003 (2009).

[20] J. M. van Ruitenbeek, A. Alvarez, I. Piñeyro, C. Grahmann, P. Joyez, M. H. Devoret, D. Esteve, and C. Urbina, Rev. Sci. Instrum. **67**, 108 (1996).

[21] D. Hazra, J. R. Kirtley, and K. Hasselbach, Appl. Phys. Lett. **104**, 152603 (2014).

[22] L. Angers, F. Chiodi, G. Montambaux, M. Ferrier, S. Guéron, H. Bouchiat, and J. C. Cuevas, Phys. Rev. B **77**, 165408 (2008).

[23] A. F. Mayadas, J. Appl. Phys. **39**, 4241 (1968).

[24] D. Gall, J. Appl. Phys. **119**, 085101 (2016).

[25] J. Charles, P. Poole, H. A. Farach, and R. J. Creswich, *Superconductivity* (Academic Press, New York, 1995).

[26] J. Romijn, T. M. Klapwijk, M. J. Renne, and J. E. Mooij, Phys. Rev. B **26**, 3648 (1982).

[27] D. Hazra, Phys. Rev. B **99**, 144505 (2019).

[28] G. J. Dolan and L. D. Jackel, Phys. Rev. Lett. **39**, 1628 (1977).

[29] K. Hasselbach, D. Mailly, and J. R. Kirtley, J. Appl. Phys. **91**, 4432 (2002).

[30] J. Clarke and A. I. Braginski, *The SQUID Handbook*, Vol. I (Wiley-VCH, Weinheim, 2004).

[31] M. Octavio, W. J. Skocpol, and M. Tinkham, Phys. Rev. B **17**, 159 (1978).

[32] D. Y. Vodolazov and F. M. Peeters, Phys. Rev. B **84**, 094511 (2011).

[33] D. Y. Vodolazov and F. M. Peeters, Phys. Rev. B **76**, 014521 (2007).

[34] G. E. Blonder, M. Tinkham, and T. M. Klapwijk, Phys. Rev. B **25**, 4515 (1982).

[35] L. Fu and C. L. Kane, Phys. Rev. Lett. **100**, 096407 (2008).

[36] E. Bocquillon, R. S. Deacon, J. Wiedenmann, P. Leubner, T. M. Klapwijk, C. Brüne, K. Ishibashi, H. Buhmann, and L. W. Molenkamp, Nat. Nanotechnol. **12**, 137 (2017).

[37] R. Fischer, J. Picó-Cortés, W. Himmler, G. Platero, M. Grifoni, D. A. Kozlov, N. N. Mikhailov, S. A. Dvoretsky, C. Strunk, and D. Weiss, Phys. Rev. Res. **4**, 013087 (2022).

[38] L. Maier, J. B. Oostinga, D. Knott, C. Brüne, P. Virtanen, G. Tkachov, E. M. Hankiewicz, C. Gould, H. Buhmann, and L. W. Molenkamp, Phys. Rev. Lett. **109**, 186806 (2012).

[39] K. Le Calvez, L. Veyrat, F. Gay, P. Plaindoux, C. B. Winkelmann, H. Courtois, and B. Sacépé, Commun. Phys. **2**, 4 (2019).

[40] G. Kunakova, T. Bauch, E. Trabaldo, J. Andzane, D. Erts, and F. Lombardi, Appl. Phys. Lett. **115**, 172601 (2019).

[41] M. Kayyalha, M. Kargarian, A. Kazakov, I. Miotkowski, V. M. Galitski, V. M. Yakovenko, L. P. Rokhinson, and Y. P. Chen, Phys. Rev. Lett. **122**, 047003 (2019).

[42] P. R. Leonid, L. Xinyu, and K. F. Jacek, Nat. Phys. **8**, 795 (2012).

[43] D. B. Szombati, S. Nadj-Perge, D. Car, S. R. Plissard, E. P. A. M. Bakkers, and L. P. Kouwenhoven, Nat. Phys. **12**, 568 (2016).

[44] K. Zuo, V. Mourik, D. B. Szombati, B. Nijholt, D. J. van Woerkom, A. Geresdi, J. Chen, V. P. Ostroukh, A. R. Akhmerov, S. R. Plissard *et al.*, Phys. Rev. Lett. **119**, 187704 (2017).

[45] J. Xiang, A. Vidan, M. Tinkham, R. M. Westervelt, and C. M. Lieber, Nat. Nanotechnol. **1**, 208 (2006).

[46] D. Montemurro, D. Stornaiuolo, D. Massarotti, D. Ercolani, L. Sorba, F. Beltram, F. Tafuri, and S. Roddaro, Nanotechnology **26**, 385302 (2015).

[47] D. Y. Vodolazov and F. M. Peeters, Phys. Rev. B **83**, 224523 (2011).

[48] M. M. Khapaev, Supercond. Sci. Technol. **10**, 521 (1997).